International Journal of Pharmaceutics 687 (2026) 126396

Contents lists available at ScienceDirect

International Journal of Pharmaceutics

journal homepage: www.elsevier.com/locate/ijpharm

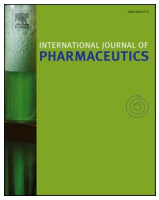

Enhancing the aqueous solubility of hemin at physiological pH through encapsulation within polyvinylpyrrolidone nanofibres

Lewis R. Anderson [a], Erum Noureen [b], Simon R. Collinson [a], Peter G. Taylor [a], Gemma C. Shearman [c], Katja Rietdorf [a], Kenneth N. White [b,*], Nicholas P. Chatterton [a,*]

[a] School of Life, Health and Chemical Sciences, The Open University, Milton Keynes MK7 6AA, UK
[b] School of Human Sciences, London Metropolitan University, London N7 8DB, UK
[c] School of Life Sciences, Pharmacy and Chemistry, Kingston University, London KT1 2EE, UK

ARTICLE INFO

Keywords:
Anaemia
Electrospinning
Solubilisation
Hemin
Self-assembly
Nanoparticles
Nanofibres

ABSTRACT

Iron deficiency anaemia is a widespread global nutritional disorder, affecting almost a quarter of the global population and contributing to impaired cognitive development, adverse pregnancy outcomes, and weakened immune function. Despite its prevalence, oral iron supplementation remains problematic due to the poor solubility and low bioavailability of ferric supplements, coupled with the frequently experienced gastrointestinal side effects associated with ferrous iron salt supplements. Hemin, a chloride-ligated ferric analogue of heme, presents a potentially safer alternative. However, its poor solubility at neutral pH limits its practical application in oral supplementation. Here, we aimed to develop a novel formulation for hemin using electrospun polyvinylpyrrolidone (PVP) nanofibres, as a platform to enhance the aqueous solubility of hemin and thereby improve its bioavailability. Hemin at various concentrations was successfully encapsulated within PVP nanofibres. The nanofibres were characterised for their morphology, physicochemical properties, encapsulation efficiency and dissolution properties. Notably, the nanofibres dissolved rapidly in phosphate-buffered saline (pH 7.4), forming hemin–PVP nanoparticles (10–80 nm in diameter) and larger aggregates (200–2000 nm in diameter) that maintained hemin in a soluble form. This approach achieved a total solubilised hemin concentration of 273 μM, representing an approximately 200-fold enhancement in solubility. These findings highlight the potential of electrospun hemin–PVP nanofibres as a promising component of an oral iron supplement, offering enhanced solubility and the potential of improved bioavailability for cellular uptake.

1. Introduction

Anaemia is a widespread global health issue which in 2021 was estimated to affect 24.3 % of the world's population and crosses all age groups (GBD 2021 Anaemia Collaborators, 2023). It commonly leads to fatigue and, in more severe cases, can result in developmental, neurological, and immunological impairments (Obeagu et al., 2025; Shah et al., 2021; Xudayberganov et al., 2017). The primary cause of anaemia is believed to be dietary iron deficiency, accounting for approximately 66 % of total cases or 1.3 billion cases globally. To maintain adequate iron levels, the human body requires daily absorption of 1–2 mg of iron from dietary sources, therefore poor dietary intake is a major contributor to iron deficiency (Auerbach et al., 2025). Iron is absorbed in the duodenum via transporter proteins expressed on the surface of epithelial cells, either in the form of ferrous iron, Fe(II), or as heme. In the case of ferric iron, Fe(III), it must first be reduced to ferrous iron by intestinal enzymes or dietary reductants such as vitamin C. Heme iron, derived from animal sources, is generally absorbed more efficiently than inorganic iron, via a mechanism still not fully understood, and its subsequent catalysed degradation by the inducible enzyme heme oxygenase-1, HO-1, frees the iron for utilisation or storage (Charlebois and Pantopoulos, 2023; Galy et al., 2024; Stec and Hinds, 2020).

Iron replacement therapy, typically administered via oral supplements, is a common treatment for iron deficiency. Most commercially available oral iron supplements are based on ferrous salts such as sulfate, fumarate, and gluconate, or ferric complexes with carriers like polysaccharides, succinate, maltol, or citrate. While ferrous salts are inexpensive, they are often poorly tolerated due to their ability to catalyse Fenton reactions, leading to gastrointestinal side effects including abdominal pain, constipation, nausea, and vomiting. Ferric salts tend to

* Corresponding authors.
E-mail addresses: kenneth.white@londonmet.ac.uk (K.N. White), nicholas.chatterton@open.ac.uk (N.P. Chatterton).

https://doi.org/10.1016/j.ijpharm.2025.126396
Received 2 October 2025; Received in revised form 4 November 2025; Accepted 13 November 2025
Available online 14 November 2025

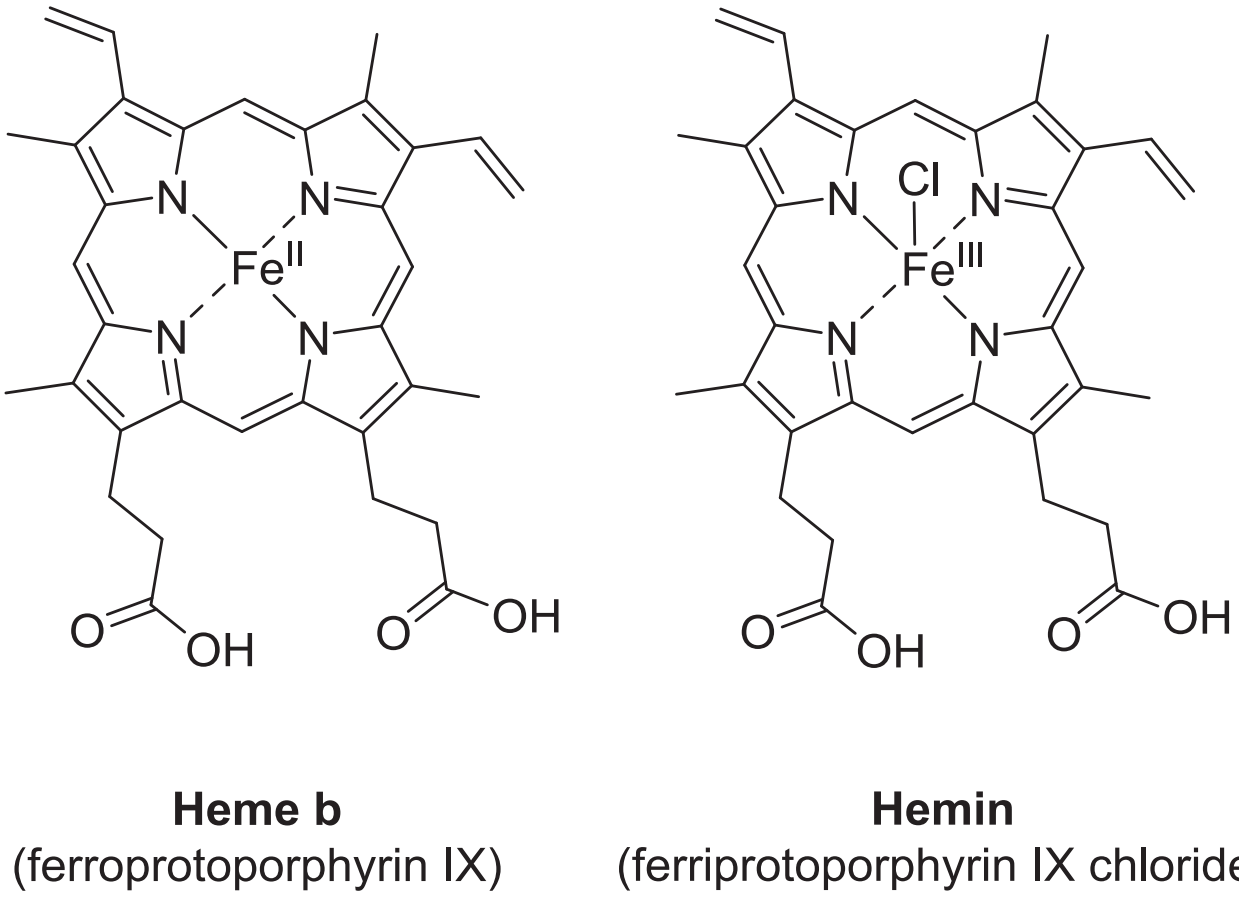

Fig. 1. The structures of Heme b and Hemin complexes.

Table 1
Previously studied hemin formulations.

Formulation	Hemin Solubility	Bioactivity	Limitations	Reference
Complexes with PEG-lactate polymer to form micelles; up to 3.9 % w/w incorporation hemin and up to 61 % encapsulation efficiency. NPs 75–140 nm.	Up to 200 μM	Ferritin increased 10x in Caco-2 cells	Polymer not commercially available; several steps in preparation; DMF:DMSO removed.	Span et al., 2016
Hemin: cyclodextrin (CD) complexes prepared in 1:2 M ratio. Encapsulation efficiency 68–72 %;	Up to 250 μM	Not toxic to IEC-6 cells up to 50 μM.	Preparation by mixing solutions of hemin and CD, drying, washing with acetone, final drying.	Yu et al., 2024
FeONP-hemin coupled compound; hydrodynamic diameter 29 nm	No data	Ferritin increased by 10x in Caco-2 cells	Four chemical steps, dialysis, repeated ultrafiltration to prepare	Jahn et al., 2011

be better tolerated but are comparatively more costly (Fütterer et al., 2013).

A recent review of 16 oral iron supplements identified only one heme-based formulation: Proferrin-ES®, a heme polypeptide complex (Pantopoulos, 2024). Despite heme's superior absorption profile compared to inorganic iron, its poor solubility and tendency to aggregate into insoluble complexes in the acidic gastric environment limit its effectiveness as an oral supplement (Hooda et al., 2014).

Hemin, a ferric protoporphyrin IX chloride, is structurally similar to heme and shares many of its physicochemical properties (Fig. 1). It is an FDA-approved drug used to treat acute intermittent porphyria, marketed under the brand name Panhematin® (Siegert and Holt, 2008). Like heme, hemin is virtually insoluble in water at neutral pH (Morrison and Williams, 1941), posing similar challenges for its oral delivery.

Nonetheless, several studies have explored strategies to formulate hemin for oral administration. As outlined in Table 1, three of these formulations include conjugation with iron oxide nanoparticles (Jahn et al., 2011), complexation with γ-cyclodextrin (Yu et al., 2024), and encapsulation within micelles (Span et al., 2016). All formulations were evaluated using intestinal cell culture models for iron uptake and toxicity, and each demonstrated potential to enhance iron absorption (Jahn et al., 2011; Span et al., 2016; Yu et al., 2024).

The dissolution of poorly water-soluble drugs has remained one of the most persistent challenges in pharmaceutics for more than half a century, with over 40 % of marketed drugs and up to 90 % of pipeline candidates exhibiting low aqueous solubility, resulting in compromised bioavailability and therapeutic performance (Kale and Shinde, 2024). Numerous formulation strategies have been explored to overcome this barrier, including solid dispersions, lipid-based systems, and nanotechnology-driven approaches (Parmar and Patel, 2025).

Among these, electrospun nanofibres have emerged as a transformative platform due to their unique physicochemical properties such as high surface area, rapid wetting, and the ability to stabilise drugs in an amorphous state, leading to significantly enhanced dissolution rates and improved absorption profiles (Castillo-Henríquez et al., 2020; Yu

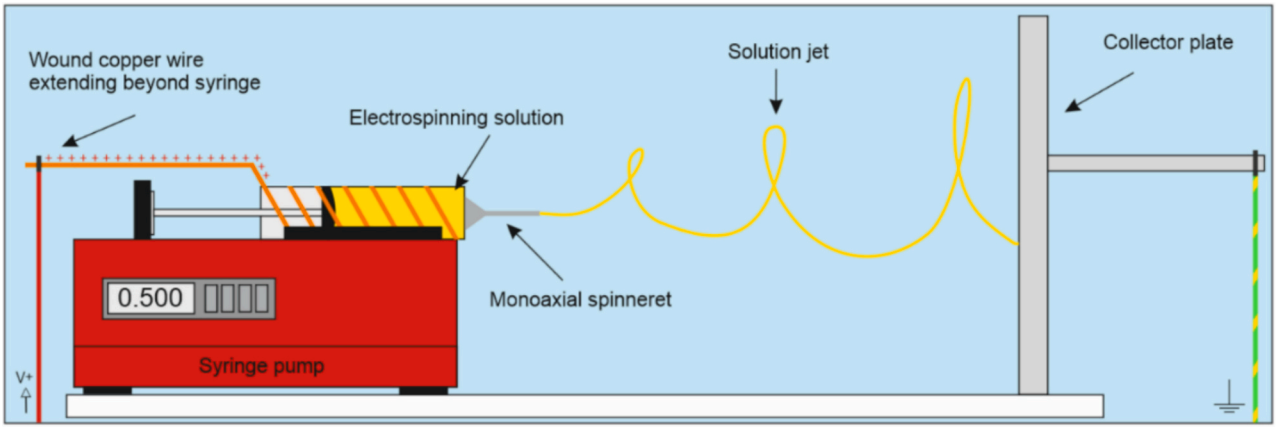

Fig. 2. Schematic diagram of the experimental set-up for extended electric field electrospinning (EEF). Figure reproduced from (Anderson et al., 2025). A photograph of the experimental set-up is shown in Fig. S1.1 (supplementary data).

et al., 2018). Beyond solubility enhancement, electrospinning offers precise control over drug release kinetics and enables patient-centric dosage forms such as fast-disintegrating oral films and localised delivery systems (Topuz and Uyar, 2025).

Therefore, an alternative way to deliver hemin could be encapsulation within a nanofibre polymer matrix to facilitate increased solubility. This study employed electrospinning of polymeric nanofibers using a modified electrospinning set-up as previously reported (Anderson et al., 2025). In conventional electrospinning, a polymer solution is passed through a syringe with a spinneret that is directly attached to a positively charged high-voltage supply, with an earthed metal collector directly opposite (Greiner and Wendorff, 2007). In the modified approach, the point of voltage supply is placed behind the electrospinning solution and needle tip, and the earthing-rod of the collector plate extended further behind the collector plate position. The resulting "extended electrical field" yields electrospinning parameters that require significantly lower power input (Anderson et al., 2025). The hydrophilic polymer polyvinylpyrrolidone (PVP) was chosen as the nanofibre matrix, as it has been shown to enhance the solubility of hemin in water (Nishide et al., 1977). A range of hemin-loaded PVP nanofibres were formulated and characterised in the solid state. On their dissolution in aqueous solution (pH 7.4), hemin-PVP nanoparticles (NPs) were found to self-assemble rapidly in solution. The formation of these NPs was found to significantly enhance the solubility of hemin within aqueous media at physiological pH. The reproducibility of nanoparticle formation from aged nanofibre formulations demonstrated in this study underscores their potential for long-term storage and on-demand preparation, aligning with the growing need for scalable, GMP-compatible manufacturing solutions in modern drug development (Omer et al., 2021; Vass et al., 2020).

2. Methods

2.1. Materials

Iron (III) chloride hexahydrate (99+%) was purchased from Acros Organics. Ethanol (EtOH, 99.8 %), hydrochloric acid (HCl, 37 %), methanol (MeOH, 99+%), and nitric acid (HNO_3, 70 %), were purchased from Fisher Scientific. *N*, *N*-dimethylformamide (DMF, 99+%) was purchased from Honeywell. Dimethyl sulfoxide (DMSO, 99.7+%), hemin chloride (96+%), phosphate buffered saline (PBS), and polyvinylpyrrolidone (PVP) (M_r = 360,000) were purchased from Sigma-Aldrich. All chemicals were used as supplied. All water was purified using a Suez Purite purification system prior to use.

Table 2
Sample identification codes and respective electrospinning parameters.

Sample code	Hemin concentration (w/w)%	Flow rate (ml hr^{-1})	Applied voltage (kV)	Humidity (%)
H0.00	0	0.4	7.5	31.5
H0.25	0.25	0.5	7.5	31.7
H0.50	0.5	0.5	8.0	33.3
H0.75	0.75	0.5	8.0	32.5
H1.00	1.0	0.5	8.0	34.0
H2.00	2.0	0.5	8.0	35.1
H3.00	3.0	0.5	8.0	34.6
H4.00	4.0	0.5	8.2	32.8
H5.00	5.0	0.5	10	31.7

2.2. Electrospinning

2.2.1. Preparation of solutions for electrospinning

15 % (w/v) stock solutions of PVP polymer were prepared by dissolving 75 g of polymer in MeOH, made up to 500 mL, with continual stirring over 24 h until fully dissolved. A second stock solution of hemin (16.67 mg mL^{-1}) was prepared in DMF. From these stock solutions,10 mL of 10 % (w/v) PVP electrospinning solutions containing hemin were prepared for a range of hemin content from 0 to 5 % (w/w), maintaining a ratio of MeOH:DMF of 7:3 by adjustment with pure MeOH or DMF as appropriate.

2.2.2. Extended electric field electrospinning (EEF)

Electrospinning solutions were transferred to a 10 mL syringe and secured onto a syringe pump (WPI AL-1010). A 1.0 mm diameter square-cut spinneret (Linari Engineering) was attached to the syringe end, with the pump arranged facing the collection plate. A copper wire (0.1 mm diameter, length *ca.* 200 mm) was secured at the spinneret base before wrapping it several times around the syringe body length. A positive voltage supply was applied to the copper wire using a 0 to 20 kV power unit (FuG Elektronik HCP 35–20000) at a position extending beyond the syringe. Additionally, a conductive steel extension was attached to the collector plate rear and earthed (Fig. 2). Nanofibres were collected onto squares of aluminium foil wrapped around the metal collection plate. Continuous electrospinning was achieved for all solutions using a tip-to-collector distance of 14 cm, at ambient temperature (24℃), and negligible current (≤ 0.0001 mA). Sample identification codes are detailed in Table 2, together with respective hemin concentration of electrospinning solutions, flow rates, and applied voltages.

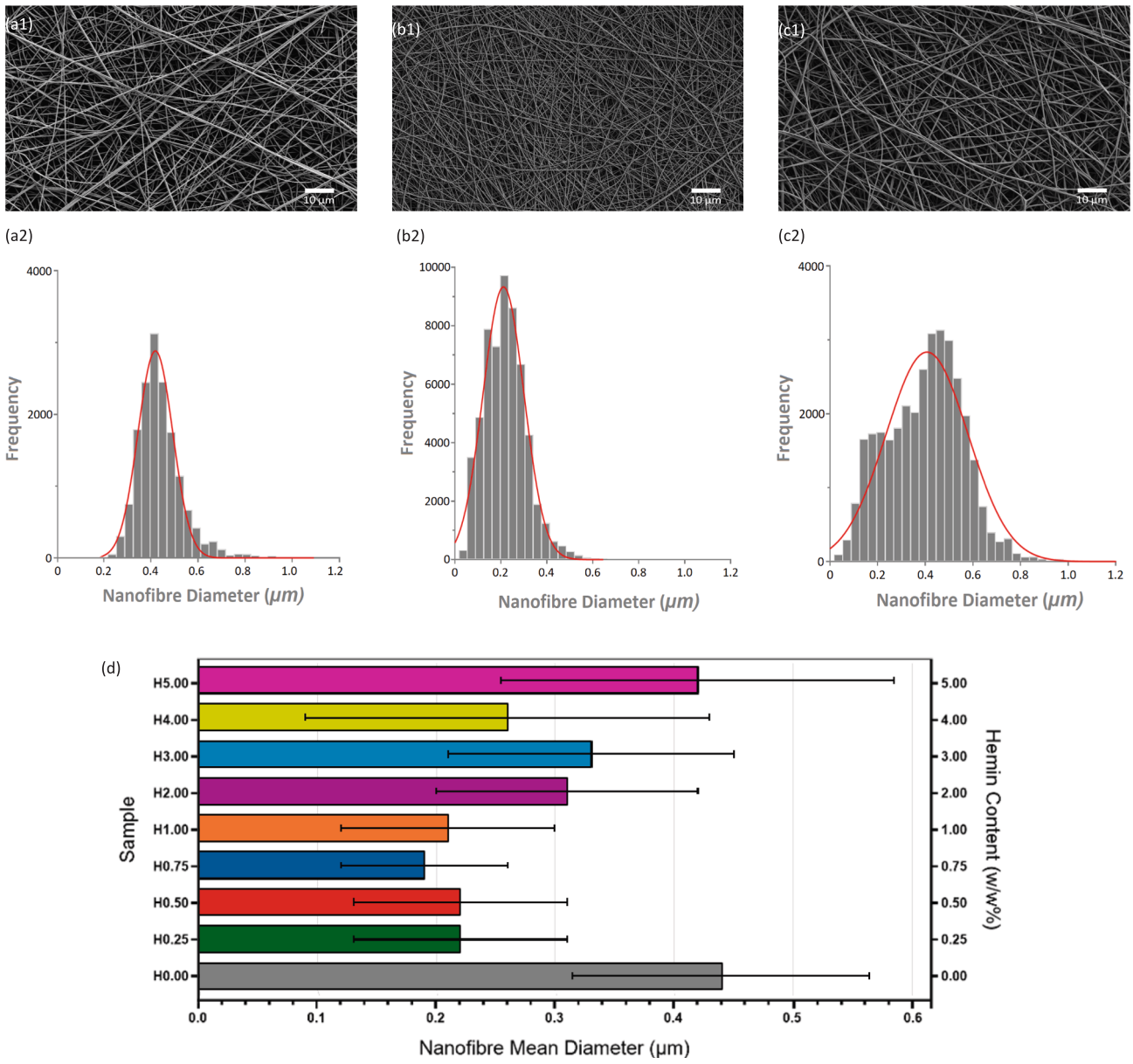

Fig. 3. (a–c) SEM micrographs of nanofibres prepared by EEF electrospinning of H0.00 (a1), H1.00 (b1), and H5.00 (c1) at 3000x magnification (scale bar 10 µm). Histograms of nanofibre diameter distributions to the respective SEM micrographs are shown under each for H0.00 (a2), H1.00 (b2), and H5.00 (c2). SEM micrographs and nanofibre diameter histograms for all formulations are shown in Fig. S2.1 (supplementary data). (d) Illustrates nanofibre mean diameters across the sample range following ImageJ analysis (DiameterJ plugin) of SEM micrograph data. Data are mean ± S.E.M diameter for 3x measurements per sample in µm Data is shown tabulated in Table S2.1 (supplementary data).

2.3. Characterisation

2.3.1. Scanning electron microscopy (SEM)

SEM was conducted on a Zeiss SUPRA 55-VP at 3 kV accelerating voltage. Samples (circa. 0.5 x 0.5 cm) were cut from each nanofibre mat, placed onto a carbon pad, and secured on a SEM specimen stub. The samples were then gold coated and imaged. Average nanofibre diameters were measured using ImageJ software (v1.52; National Institutes of Health) and the DiameterJ plugin (Hotaling et al., 2015).

2.3.2. Transmission electron microscopy (TEM)

TEM was conducted on a JEM-1400 (JEOL). Nanofibres were directly spun onto carbon-coated copper TEM grids (TAAB) held at the collector plate for 40 s during electrospinning. Nanoparticles (NPs) prepared from dissolved fibres were dialysed against water over a period of 5 days, with daily changes of water, using 3.5 kDa MWCO SnakeSkin™ dialysis tubing (Thermo Scientific) to remove salts from the dissolution media. Samples of dialysed NPs were pipetted onto holey carbon-coated copper TEM grids and left to dry for 2 h before imaging.

2.3.3. Energy dispersive X-ray (EDX)

EDX mapping was achieved on a JEM-2100 (JEOL) using an AMETEK EDAX TSL set at 200 kV and magnification x250,000.

2.3.4. Simultaneous thermal analysis (STA)

STA was performed on a Rheometric Scientific STA 1500 system (Rheometric Scientific Ltd). Samples (5–20 mg) were placed within aluminium crucibles (40 µL) and secured within the STA instrument balance. Once the system was sealed and settled (30 s) the sample weight was measured before running STA at the following settings: N_2 (30 mL min^{-1}), ramp to 600 °C at 10 °C min^{-1}.

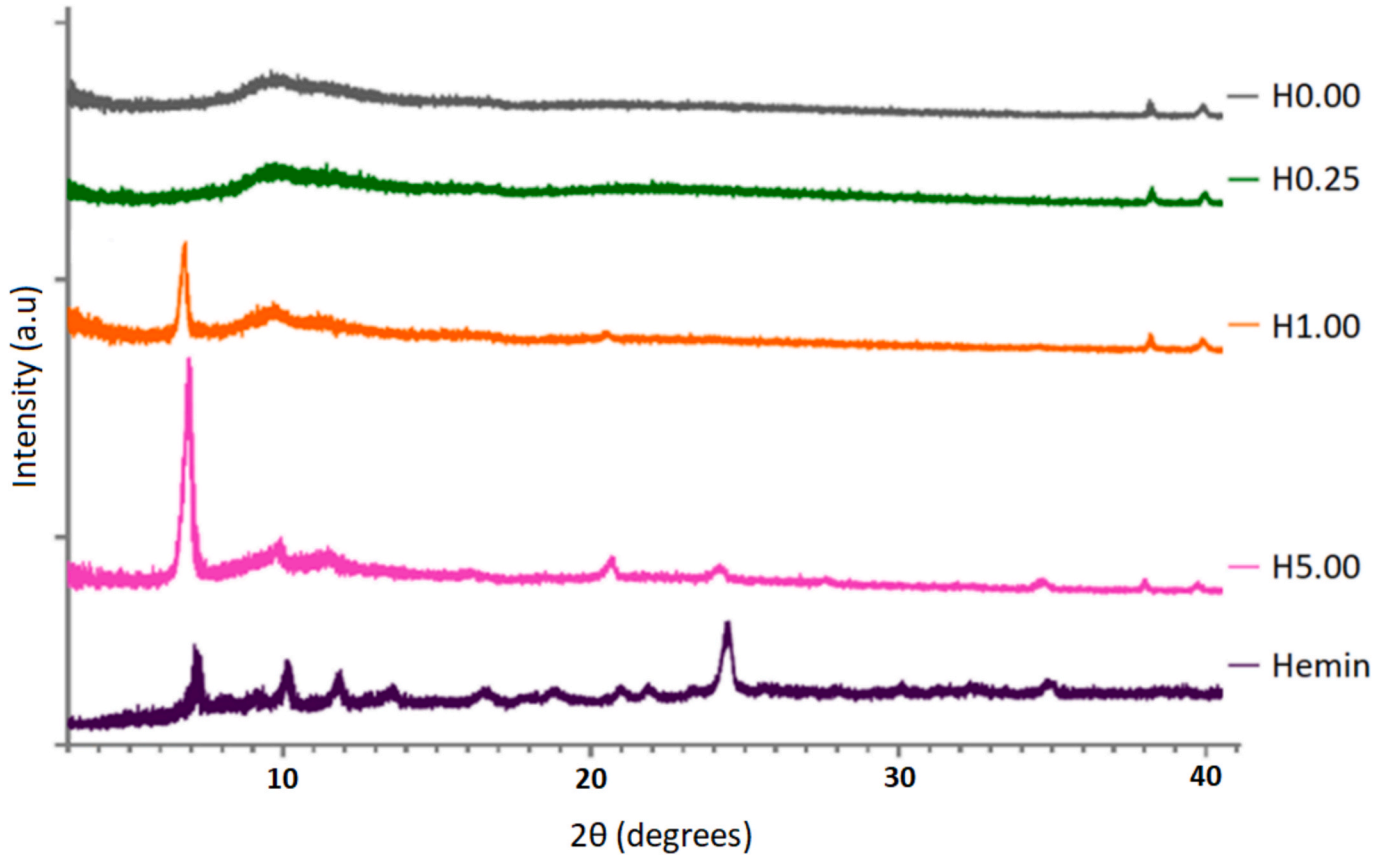

Fig. 4. XRD diffraction patterns of H0.00, H0.25, H1.00, H5.00, and hemin powder (Hemin). XRD diffraction patterns for formulations H0.50, H0.75, and hemin:PVP (1:99) physical powder mixture (HPX) is shown in Fig. S4.1 (supplementary data).

2.3.5. Fourier transform infrared spectroscopy (FTIR)

FTIR spectra were obtained using a Thermo Nicolet NEXUS 470 FTIR over the wavenumber range 700–4000 cm^{-1} and with resolution of 4 cm^{-1}.

2.3.6. X-ray diffraction (XRD)

XRD analysis of fibres and chemicals was conducted on a Rigaku Miniflex 600 instrument. Nanofibre samples were cut to sample holder disk size. Powder reagents and samples were spread evenly across the sample holder. XRD parameters used were; Cu-Kα radiation (λ = 0.15418 nm; 40 kV; 15 mA). Patterns were recorded over the 2θ range from 3° to 50° at 2.5° min^{-1} in 0.01° steps.

2.3.7. Dynamic light scattering (DLS)

DLS was obtained with a Nanotrac flex (Microtrac Retsch GmbH). Sample solutions (10 mL) were probed with the Nanotrac flex sensor and intensity measurements performed over 30 s per measurement. The data presented is the mean of 10x replicate measurements per sample.

2.4. Dissolution studies

2.4.1. Nanofibre dissolution

Dissolution tests were conducted on hemin-PVP nanofibre samples (65.2 mg) added to isotonic PBS (10 mL), before stirring between time ranges of 1 h to 72 h. Sample aliquots were drawn from the solution at volumes required for respective analysis.

2.4.2. Physical-mixture dissolution

Hemin powder was added to pre-dissolved PVP within a beaker of PBS (10 mL), maintaining total mass content of 65.2 mg 10 mL^{-1}, at hemin:PVP ratios; 0:100, 0.1:99.9, 0.25:99.75, 0.5:99.5, 0.75:99.25, 1.0:99.0, and 5.0:95.0. The mixtures were continually stirred over 72 h. Sample aliquots were drawn from the solution at volumes required for respective analysis.

2.4.3. UV–vis spectroscopy

The UV–visible spectra of hemin preparations were obtained using a JASCO V-530 spectrophotometer over a wavelength range of 250–700 nm.

2.4.4. Inductively coupled plasma optical emission spectroscopy (ICP-OES)

The iron content of dissolved fibre solutions was measured by ICP-OES using an Agilent 5110 instrument. Dissolution aliquots of each sample and repeats were diluted 10x with 0.3 M HNO_3. Final iron concentrations were corrected for dilution of dissolution volume.

2.5. Statistical analysis

GraphPad PRISM 9 software was used for graphical representation and statistical analysis. Outliers were removed for all datasets before D'Agostino & Pearson and Shapiro-Wilk tests for assessment of normal distribution. The data are presented within charts representing the mean of each datapoint and error bars representing the standard error of the mean (±S.E.M). Parametric comparison between two datasets was performed using one-way ANOVA and comparison between three, or more, datasets was performed using two-way ANOVA.

3. Results

3.1. Hemin-loaded PVP nanofibres

Homogeneous PVP fibres containing hemin from 0.25 % to 5 % (w/

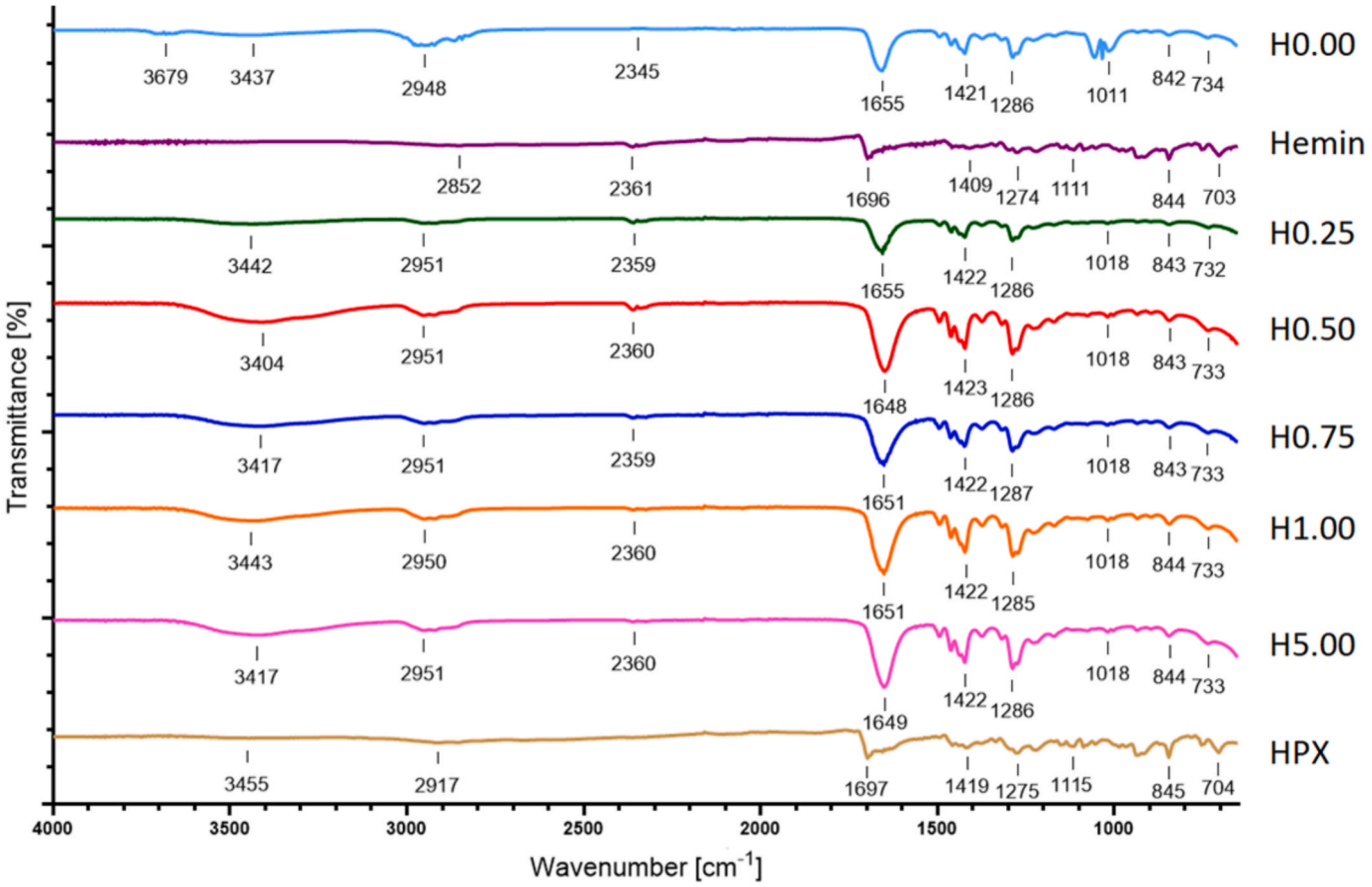

Fig. 5. FTIR spectra of blank PVP nanofibres (H0.00), PVP powder (PVP), hemin powder (Hemin), H0.25, H0.50, H0.75, H1.00, H5.00, and hemin:PVP (1:99) physical powder mixture (HPX).

w) were prepared readily using extended electric field electrospinning (EEF). The proportion of hemin incorporated into the nanofibres was limited by the relatively low solubility of hemin in DMF, and the requirement to use compatible solvents for electrospinning, therefore an electrospinning solution of 5 % (w/w) hemin was a practical maximum concentration. Representative SEM micrographs of nanofibres prepared via EEF electrospinning, along with histograms of their diameter distributions, are presented in Fig. 3(a-c). Additional formulations are shown in the supplementary data (Fig. S2.1). Across all hemin concentrations, the nanofibres appeared visually smooth and well-formed. The histograms reveal a relatively narrow diameter distribution at low or no hemin concentrations, which progressively broadens with increasing hemin content, up to 5 % (w/w).

Fig. 3(d) compares the diameters of nanofibres produced at the varying hemin loadings. Previous studies have reported that increasing hemin concentration tends to reduce fibre diameter (Tyubaeva et al., 2024, 2023), likely due to enhanced conductivity of the electrospinning solutions. A similar trend is observed in samples H0.00 to H1.00. However, at higher hemin concentrations (e.g., H5.00), an increase in mean fibre diameter is noted, which may be attributed to the different polymer system used in this study.

Transmission electron microscopy (TEM) imaging and energy-dispersive X-ray (EDX) mapping of sample H1.00 were performed to examine morphology at higher magnification and to detect the distribution of iron within the nanofibre (Fig. S3.1, supplementary data). Iron signals were detected along the nanofibre path suggesting that hemin molecules are relatively well encapsulated and uniformly distributed. Subsequent X-ray diffraction (XRD) analysis (Fig. 4) revealed that hemin was amorphously dispersed within nanofibres at lower concentrations (0.25–0.75 % w/w; samples H0.25 to H0.75, Fig. S4.1, supplementary data). However, at higher hemin loadings (1.0 and 5.0 % w/w; samples H1.00 and H5.00), a prominent diffraction peak at approximately 6.5° was observed, along with several smaller but distinct peaks at higher 2θ values. These features are indicative of crystalline hemin domains forming within the nanofibre matrix at elevated concentrations.

Increased hemin crystallinity at higher concentrations has been observed previously (Tyubaeva et al., 2024), most likely due to the tendency of hemin to aggregate in the solution feed at larger measures (Golnak et al., 2015). Here, the strong small angle reflection *ca.* 6.5° is likely due to long-range ordering of the porphyrin rings in the nanofibre formulation, as this peak intensifies in correlation with increased hemin concentration (comparing H1.00 with H5.00).

The increase in crystallinity/aggregation of hemin at higher concentrations is potentially reflected in the FTIR spectra of the formulations (Fig. 5). Increasing hemin concentration is seen to reduce the PVP C=O stretching frequency from 1655 cm^{-1} for H0.25 shifting to 1649 cm^{-1} in sample H5.00. This red-shift could be due to enhanced H-bonding between the carboxylic acid groups in the hemin aggregate and the carbonyl groups of PVP (Aljabri et al., 2019; Taylor and Zografi, 1997). When hemin powder and PVP powder are physically mixed in a 1:99 ratio (“HPX”), mimicking the theoretical composition of sample H1.00, characteristic hemin vibrations C=O (1697 cm^{-1}), C–N (1275 cm^{-1}), and C–O (1115 cm^{-1}) are identifiable, comparable to those observed in pure hemin powder. In contrast, these bands are absent in sample H1.00, supporting the hypothesis that electrospinning promotes effective encapsulation of hemin, and red-shift of hemin’s C=O stretching frequencies following H-bonding.

Differential scanning calorimetry (DSC) and thermogravimetric analysis (TGA) of hemin and the polymer composites as powder or as nanofibres is shown in Fig. 6. The thermal analysis of hemin shows it is

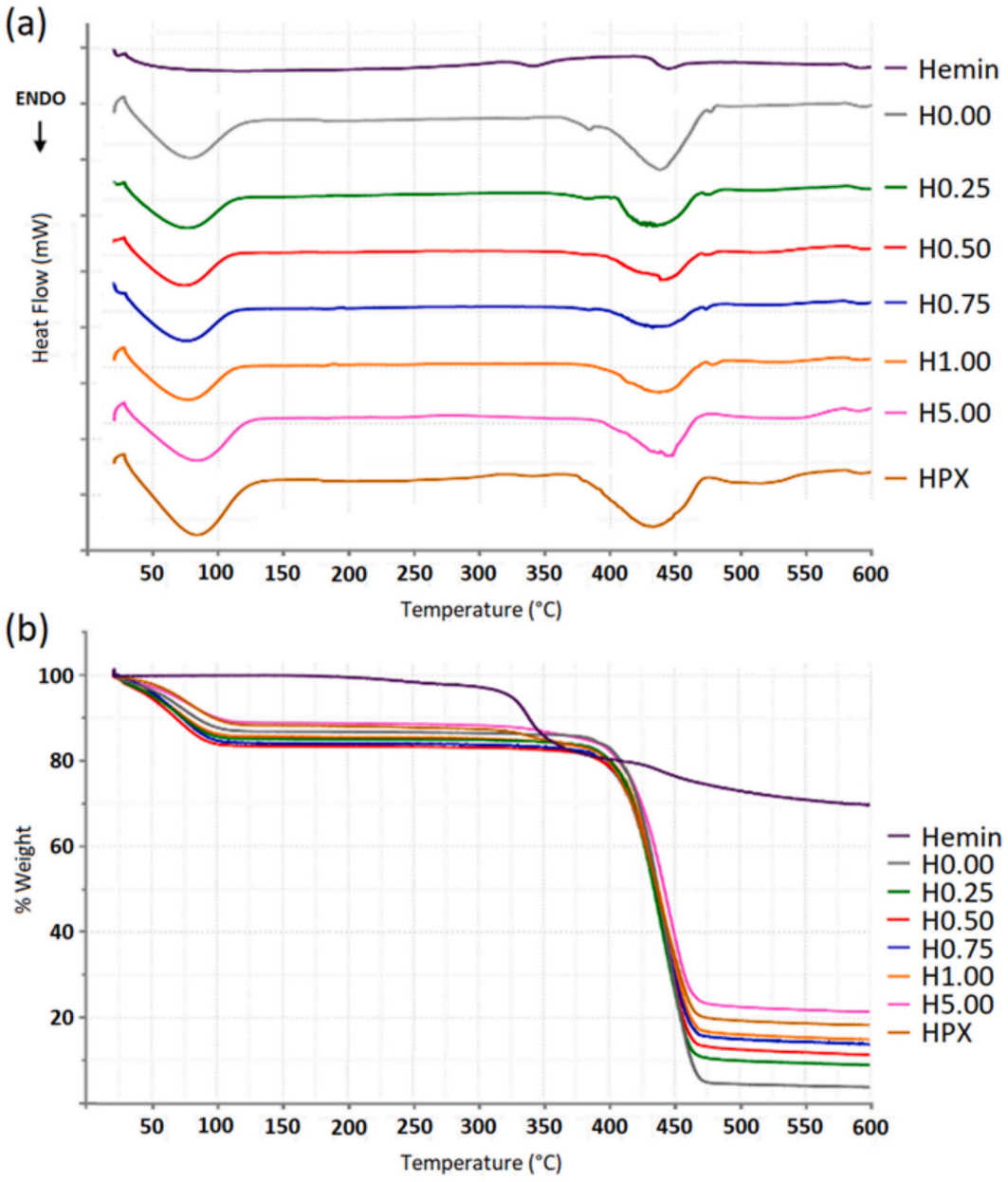

Fig. 6. DSC (a) and TGA (b) analysis of hemin powder (Hemin), blank PVP nanofibres (H0.00), hemin-loaded PVP monoaxial nanofibre samples (H0.25, H0.50, H0.75, H1.00, and H5.00), and hemin:PVP (1:99) physical powder mixture (HPX).

stable up to about 320 °C. The small endotherm peak measured by DSC at ~ 340 °C (Fig. 6a) corresponds to weight loss measured by TGA (Fig. 6b) at the same temperature, possibly owing to decarboxylation of the acid groups and loss of two CO_2 for each hemin complex. The high residual mass observed for hemin (~70 %) by the TGA is likely due to the formation of complex organometallic species including polymers (rather than iron oxides) as the thermal analysis was conducted under nitrogen (Said and Al-Sammerrai, 1985). The DSC data of the polymer materials reveals a broad endothermic peak between 50 and 100 °C, attributed to evaporation, and a second endothermic peak around 400–450 °C corresponding to substantial weight loss as the polymer decomposes.

This endotherm incrementally shifts to a slightly higher temperature with increasing hemin content, potentially owing to greater hemin crystallinity in alignment with the XRD findings. However, further investigation is required to understand this observed effect of hemin loading on thermal behaviour. The residual masses increase broadly in line with expected hemin loading, however due to the complexity of the residual products formed (Said and Al-Sammerrai, 1985), these masses cannot be used to estimate hemin content in the fibre formulations. In sample HPX there is small endotherm *ca.* 170 ℃ due to the transition from glassy to state to the rubbery state (Dong et al., 2024) – this transition is surprisingly still present in the electrospun materials (Fig. S5.1). We speculate that ordering of the hemin molecules in our electrospun nanocomposites has influenced this thermal behaviour, perhaps by encouraging segmental motion of the polymer chain (Bailey and Winey, 2020).

The TGA data in Fig. 6(b) indicate that the nanofibre samples exhibit thermal stability up to approximately 300 °C, beyond which decomposition begins as evidenced by weight loss. This suggests that the nanofibres are thermally stable. To assess their long-term stability under ambient conditions, samples H0.00 to H5.00 were stored in a sealed

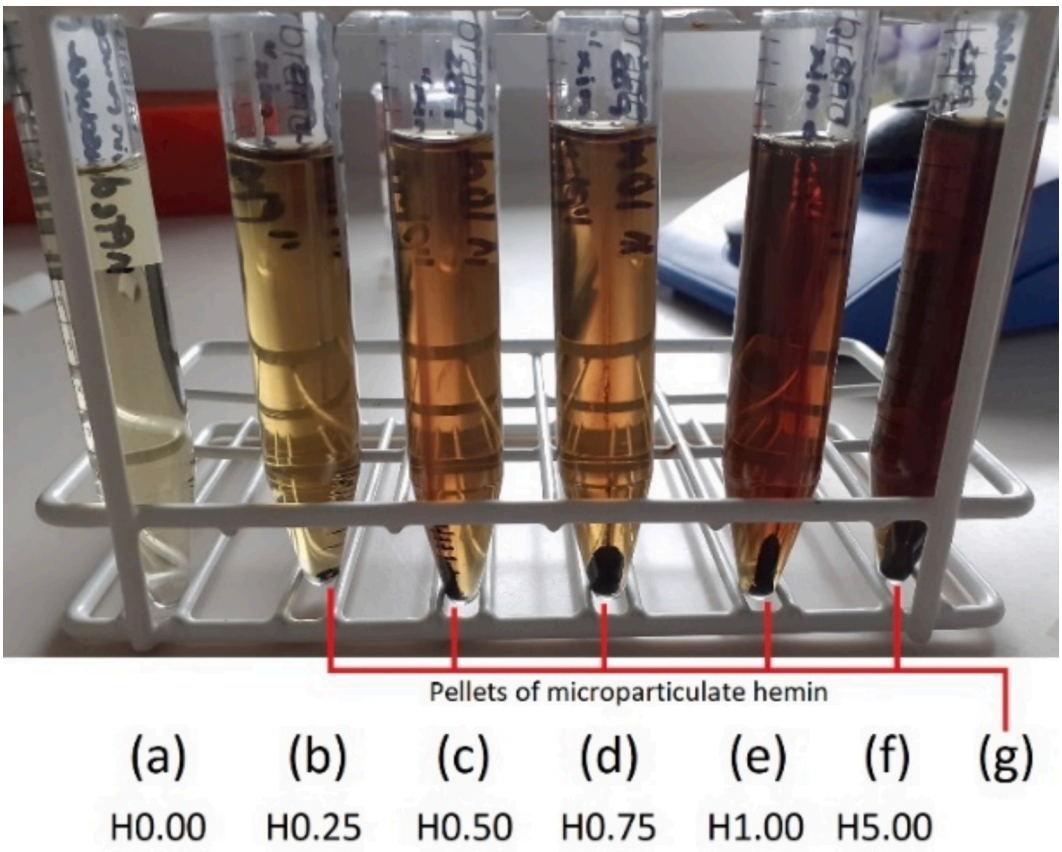

Fig. 7. PBS solutions of dissolved nanofibre formulations H0.00 (a), H0.25 (b), H0.50 (c), H0.75 (d), H1.00 (e), and H5.00 (f) (65.2 mg of each sample in 10 mL PBS), with thin layers of smeared microparticulate hemin pellets at the falcon tube conical tip (g).

container within a cool, dark cupboard for 24 months. As expected, due to the hygroscopic nature of PVP, XRD analysis of the aged samples revealed broadening of the amorphous halo across all formulations (Fig. S6.1), consistent with water uptake. This observation aligns with previous studies showing diffraction curve changes in PVP corresponding to oxygen–oxygen distances in absorbed water molecules (Benmore et al., 2023).

Samples with higher hemin loadings (1.0 and 5.0 % w/w; H1.00 and H5.00) retained the characteristic diffraction peak at ~ 6.5°, along with weaker peaks at higher 2θ values indicative of crystalline hemin domains. However, the intensities of these peaks were markedly reduced compared to freshly prepared samples, suggesting a loss of crystallinity likely due to water-induced plasticisation and increased polymer chain mobility disrupting long-range order.

FTIR analysis further confirmed water absorption over the 24-month period, showing up to a 17 % decrease in O–H stretching band transmittance (3700–3100 cm^{-1}) and red-shifts of several cm^{-1} in the C=O stretching bands across all samples (Fig. S6.2). These shifts reflect hydrogen bonding between PVP's carbonyl groups and absorbed water (Mishra et al., 2008).

Despite these changes, SEM imaging after the 24 month-period revealed well-formed cylindrical fibres with diameters comparable to their freshly prepared counterparts (Fig. S6.3). These findings confirm that while atmospheric moisture was absorbed, no significant structural damage or defects were observed. Notably, the nanofibres returned to their original state after overnight drying at 30 °C, indicating reversible moisture effects.

3.2. Nanofibre dissolution studies

Samples of hemin nanofibres (65.2 mg in each case) were dissolved in PBS (10 mL) at room temperature. All nanofibre samples dissolved completely within 1 h, producing green–brown solutions of increasing intensity with increasing hemin concentration (Fig. 7(a-f)). Precipitation of microparticulate hemin was observed in small amounts after stirring for 1 h, which could be collected by pelleting through centrifugation (Fig. 7(g)). UV–Vis measurement at 396 nm of sample H1.00 during dissolution reveals that equilibrium solubility is reached within 30 min, as no further increase in maximum absorbance is observed even when stirring is continued for up to 72 h (Fig. S7.1). As a comparative study, physical mixtures were prepared by adding hemin powder to pre-dissolved PVP in PBS, using the same hemin:PVP weight % ratios as the hemin-PVP nanofibres (0:99 to 5.0:95.0). After one hour of stirring, no noticeable colour change was observed, in contrast to the swift colour changes seen upon nanofibre dissolution. The mixtures were left under continuous stirring, with slight colour changes emerging after 24 h. These changes gradually intensified over time. After 72 h of stirring, no further deepening of colour was observed, and the mixtures visually resembled their corresponding hemin-PVP nanofibre solutions as illustrated in Fig. S8.1 (supplementary data).

Fig. 8 shows the UV–visible spectra of dissolved nanofibres and hemin powder in PBS. All hemin-loaded nanofibre samples exhibit a broad Soret peak (around 390 nm), indicative of hemin dimerization (Nath et al., 2017). The λ_{max} peaks for dissolved hemin-PVP fibres are in the Soret band, as is the case for hemin powder (387.5 nm) (Fig. 8). The λ_{max} for the nanofibre formulations shift hypsochromically with increasing hemin concentration; H0.25 (395.0 nm), H0.50 (394.0 nm), H0.75 (394.0 nm), H1.00 (393.5 nm), and H5.00 (392.5 nm). This blue

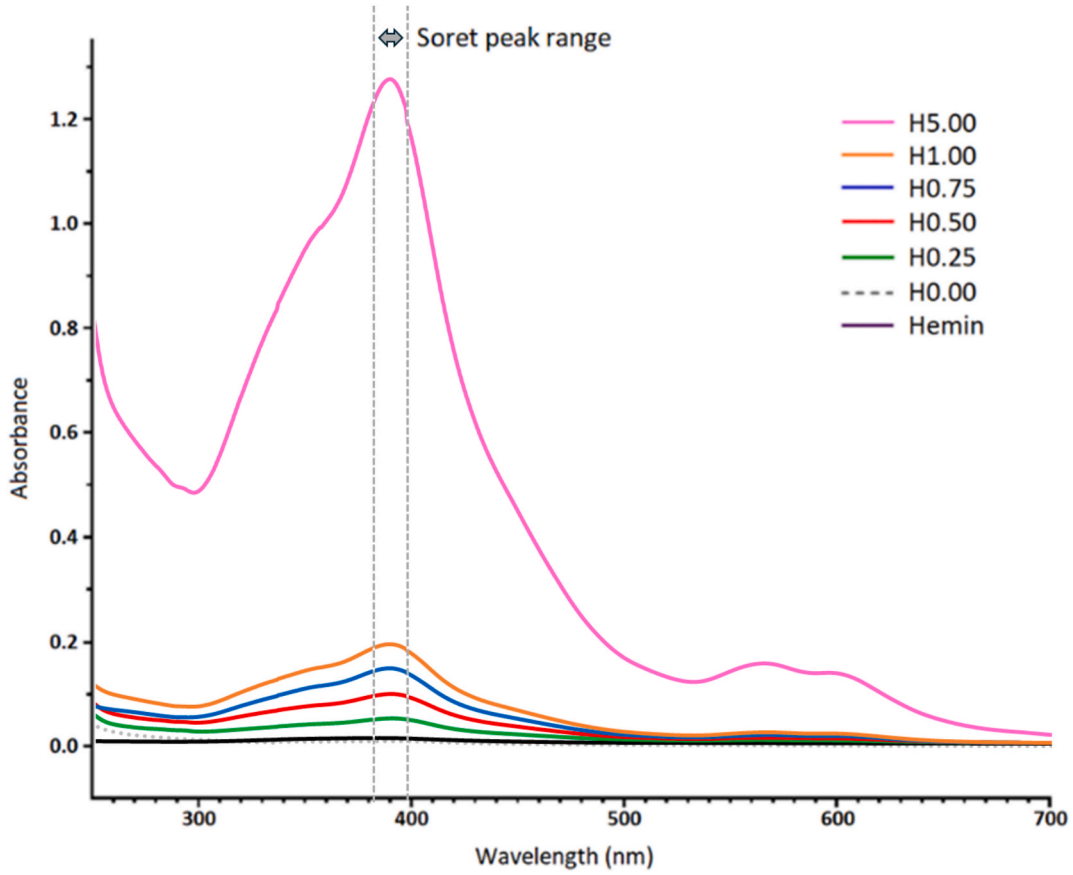

Fig. 8. UV–visible spectra for hemin powder (1.00 mg), H0.00, H0.25, H0.50, H0.75, H1.00, and H5.00 (65.2 mg for each nanofibre sample) in PBS (10 mL), post-centrifugation.

shift is possibly an effect of increasing hemin H-aggregation, the face-to-face arrangement of porphyrin π–π stacking, as the Soret peak intensities increase linearly (Suzuki et al., 2016).

Dissolved samples of nanofibre solutions were analysed for their iron content by ICP-OES (Fig. 9). Samples were analysed before and after centrifugation to quantify the level of both soluble and insoluble iron (Fig. 9(a), left y-axis). The level of insoluble iron was low for samples H0.25 to H3.00 making only small, statistically insignificant, differences to the concentration of soluble hemin before and after centrifuging. In comparison, solutions of H4.00 and H5.00 had 5–10 % less hemin after centrifugation. An indication of encapsulation efficiency (EE) is given by % iron measured in the dissolved nanofibre solutions against the theoretical maximum iron concentration within the nanofibres, calculated from the known hemin concentrations within the original electrospinning solutions (100 %, Fig. 9(a), right y-axis), measuring from ~ 35 % for H1.00 fibres to ~ 80 % for H0.25 and H5.00. Due to the higher solubility of hemin within DMSO to that of aqueous media, EE was measured more precisely by dissolving the nanofibre samples in DMSO and measuring Fe content of solutions by ICP-OES (Fig. 9(b)).

The DMSO solutions were free of particulate Fe and the EE's ranged from 43 % to 83 %, with the highest achieved from nanofibres with the lowest proportion of hemin, H0.25. The hemin-PVP nanofibres were able to facilitate enhanced aqueous solubility (Fig. 10) with approximately 200-fold increased solubilised Fe (H5.00, pH 7.4, PBS) in comparison with hemin alone in the same media. The concentration of soluble hemin prepared from nanofibres increased as the content of hemin in the nanofibre increased, with dissolved H5.00 creating a solution of *ca.* 273 μM.

The markedly enhanced aqueous solubility of hemin in these solutions suggested the possibility of soluble nanoparticle formation (Inamura et al., 1989). Each of the PBS solutions containing dissolved nanofibres was analysed by DLS (Fig. 11). All samples dissolved to create a distribution of nano-sized particles between 10–100 nm diameter (median diameter range 20–40 nm). For all samples, there are also populations of larger nanoparticles. However, the proportion of smaller nanoparticles decreased as the content of hemin increased, and the proportions of larger-sized particles grew correspondingly.

PVP is known to solubilise porphyrins and related molecules, including chlorin-type photosensitizers, through the formation of nanoparticles (Paul et al., 2013). The two driving forces for this process are a) hydrophobic interactions involving the C–H moieties on the polymer backbone, and non-polar regions of the solute on the interior of the nanoparticle and b) hydrogen bonds between the exposed carbonyl groups on PVP and solvent water molecules (Tsvetkov et al., 2014). We presume similar processes are at play when the nanofibre samples described here dissolve. Aggregation of PVP NPs loaded with chlorins has also been observed previously (Batov et al., 2019). We speculate that that extent of hemin aggregation in the nanofibre samples plays a role in the various NP populations observed in the DLS.

Time-resolved DLS measurements were attempted to monitor nanoparticle formation during nanofibre dissolution. However, these proved unreliable for due the presence of large particles which obscure the signal from the small particles. Based on combined XRD, UV–Vis, and DLS data recorded, Fig. 12 provides a summary of the potential factors which influence the varying nanoparticle populations when the different formulations are dissolved in aqueous media.

Samples with low hemin loading most probably contain dispersed hemin molecules, which are released upon dissolution in PBS generating nanoparticles of small diameter. Molecular interactions between hemin and PVP promote association leading to formation of nanoparticles that

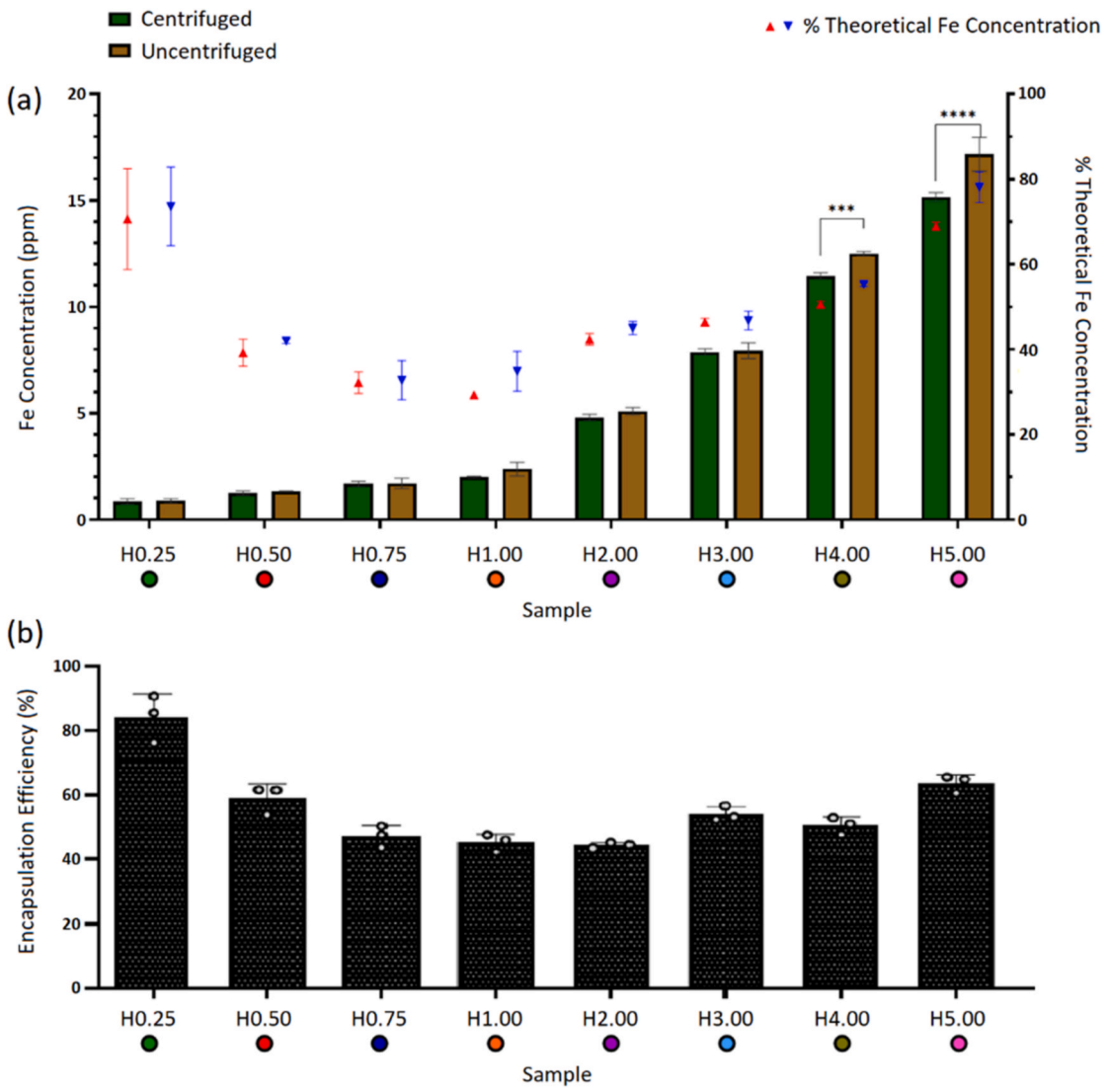

Fig. 9. (a) Fe concentration (ppm) (left y-axis) of centrifuged (green) and uncentrifuged (brown) nanofibre samples (H0.25, H0.50, H0.75, H1.00, H2.00, H3.00, H4.00, and H5.00) dissolved in PBS, together with % of theoretical iron concentration (right y-axis) for centrifuged (red arrows) and uncentrifuged (blue arrows) samples. Data were analysed with two-way ANOVA comparing mean centrifuged iron and mean uncentrifuged iron within each formulation, where **** = $p < 0.0001$, *** = $p < 0.0003$, n = 3, data are the mean ± S.E.M for three independent preparations and measurements. (b) Encapsulation efficiency of hemin in fibres. Iron concentration (ppm) was measured in solutions of 65.2 mg of fibres in 10 mL DMSO by ICP-OES. Data are expressed as the % ratio of measured / expected iron.

shield the hemin complex from the aqueous environment in similar manner to that described previously (Tsvetkov et al., 2014).. These small nanoparticles can further associate into larger aggregates (~400 nm).

The hemin-loaded nanofibres with intermediate loading (0.75–2.00 % w/w) exhibit some hemin aggregation, as supported by XRD and UV–Vis analysis. This may be providing larger nucleation sites for PVP association during nanofibre dissolution, producing larger nanoparticles (~450 nm), especially when multiple hemin clusters are encapsulated within a single particle. These nanoparticles also aggregate into larger structures (~2000 nm) that still preserve solubility within the PBS solution.

Nanofibres with ≥ 3.00 % w/w hemin appear even more crystalline in XRD, so are likely to form even larger nucleation centres for PVP association. This results in nanoparticles (~500 nm) that aggregate into soluble populations around 1500 nm. Overall, this suggests a dynamic system where increasing hemin concentration drives greater hemin aggregation during electrospinning, creating larger nucleation sites and leading to three distinct nanoparticle size distributions, with aggregate size correlating with hemin content.

DLS measurements of the hemin:PVP physical mixtures provide further insight (Fig. S9.1, Table S9.2, supplementary data). Although nanoparticle formation required over 72 h of continuous stirring following hemin powder addition to pre-dissolved PVP, the emergence of similarly coloured solutions to those of the dissolved nanofibres suggested comparable nanoparticle generation. For mixtures with hemin:PVP ratios equivalent to H0.25 through H5.00, the majority of nanoparticles formed were between 200–2000 nm in diameter (≥ 64 %), with only minor populations observed in the 10–80 nm range (≤ 23 %) – unlike the low hemin-loaded nanofibre samples themselves, H0.25-H0.75, which predominantly yielded sub-100 nm particles. This disparity likely arises from the high levels of aggregated and insoluble hemin in the physical mixtures, which may provide larger nucleation sites for PVP association and subsequent nanoparticle formation. This highlights the advantage of the dispersed hemin content in lower-loaded nanofibres, where their dissolution promotes the formation of smaller nanoparticles. These findings suggest that the physical state and dispersion of hemin prior to nanoparticle formation play a critical role in determining particle size, with nanofibre dissolution offering a more controlled route to sub-100 nm particles.

Transmission electron microscopy (TEM) was used to further

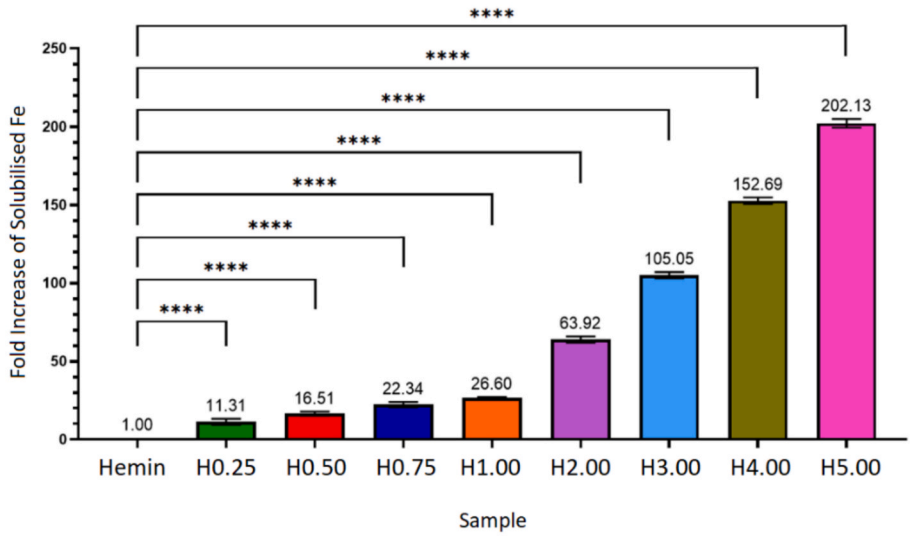

Fig. 10. Fold increase of hemin solubility within centrifuged hemin-loaded PVP nanofibres dissolved in PBS dissolutions against reported hemin solubility (0.9 mg L^{-1}) (Morrison and Williams, 1941), based on data from Fig. 9(a). Data were analysed with one-way ANOVA comparing the difference between soluble iron of all formulations against raw iron (of hemin) solubility, where **** = $p < 0.0001$, n = 3, data are the mean ± S.E.M for three independent preparations and measurements.

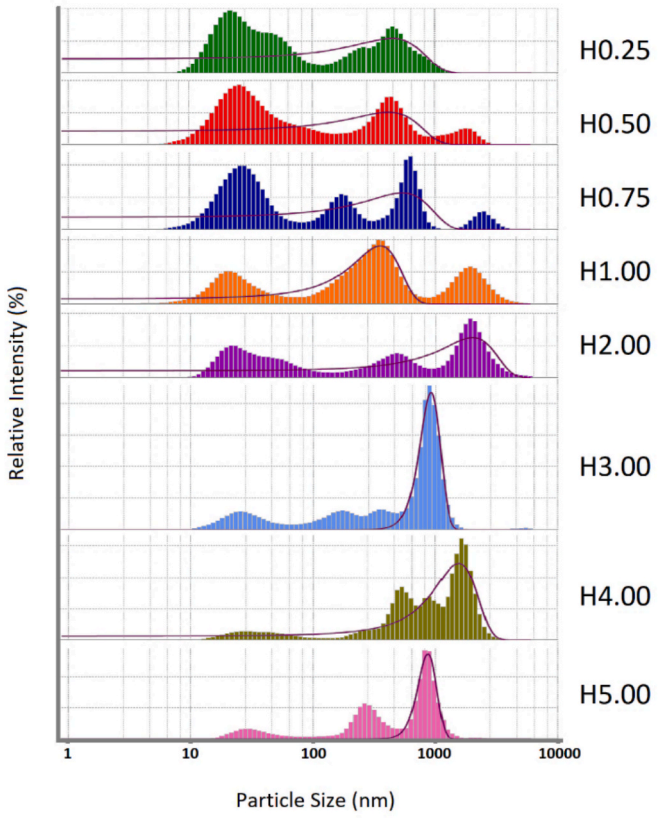

Fig. 11. DLS histograms of particle size populations found in PBS solutions of dissolved hemin-PVP nanofibres (H0.25-H5.00), following centrifugation. Purple lines represent overall distribution curve for pooled particle sizes. Measurements are mean particle size distributions of 10x measurements per sample. Tabulated data including standard deviations and polydispersive indexes (PDI) is shown in Table S8.1 (supplementary data).

characterise the self-assembled nanoparticles following nanofibre dissolution (Fig. 13). Two visually distinct nanoparticle populations were observed in each sample. TEM micrographs in the top two windows of each panel (Fig. 13(a–f1) and (a–f2)) show irregular clusters composed of small, dense, asymmetrical nanoparticles with a mean diameter of 44.3 ± 17.1 nm (n = 213), corresponding to the smallest size distribution (10–80 nm) measured by DLS (Fig. 11). A second population, visible in the bottom two windows (Fig. 13(a–f3) and (a–f4)), consists of larger, more spherical particles with a mean diameter of 198.0 ± 25.3 nm (n = 255), aligning more with the second largest population observed in the DLS.

In the higher concentration samples (H1.00, H3.00, and H5.00), increased agglomeration of this second largest type was observed, potentially correlating with the largest diameter population observed in the DLS (Fig. 11). This trend suggests that increasing hemin concentration promotes the formation of larger particles, consistent with Langmuir-type adsorption dynamics in which saturation of polymer–drug interactions reduce encapsulation efficiency and promotes aggregation to form larger particles (Lee et al., 2021).

Additionally, EDX was used to map iron signals within the nanoparticles (Fig. S10.1, supplementary data). Iron signals were found throughout the map surface, but a small majority of the signal, 59 %, was found within the boundaries of nanoparticles, suggesting the presence of hemin within. The presence of Fe signals outside the boundaries of the particles could be due to the loss of hemin-PVP complexes from the nanoparticles, rather than free hemin which would have been removed during dialysis.

To assess the reproducibility of hemin-PVP nanoparticle formation, the 24-month aged samples previously discussed in Section 3.1 were placed in PBS (65.2 mg 10 mL-1) and stirred over 1 h. Aged samples of H0.25, H1.00, and H5.00 were dissolved in the same manor as their freshly prepared counterparts, as previously detailed within Section 3.2, producing comparable hemin-PVP nanoparticle populations (Fig. S11.1 (a-c), supplementary data). This confirms that the nanoparticle formation process is reproducible even after prolonged storage, indicating that the structural integrity of the hemin–PVP nanofibre formulations is maintained over 24 months.

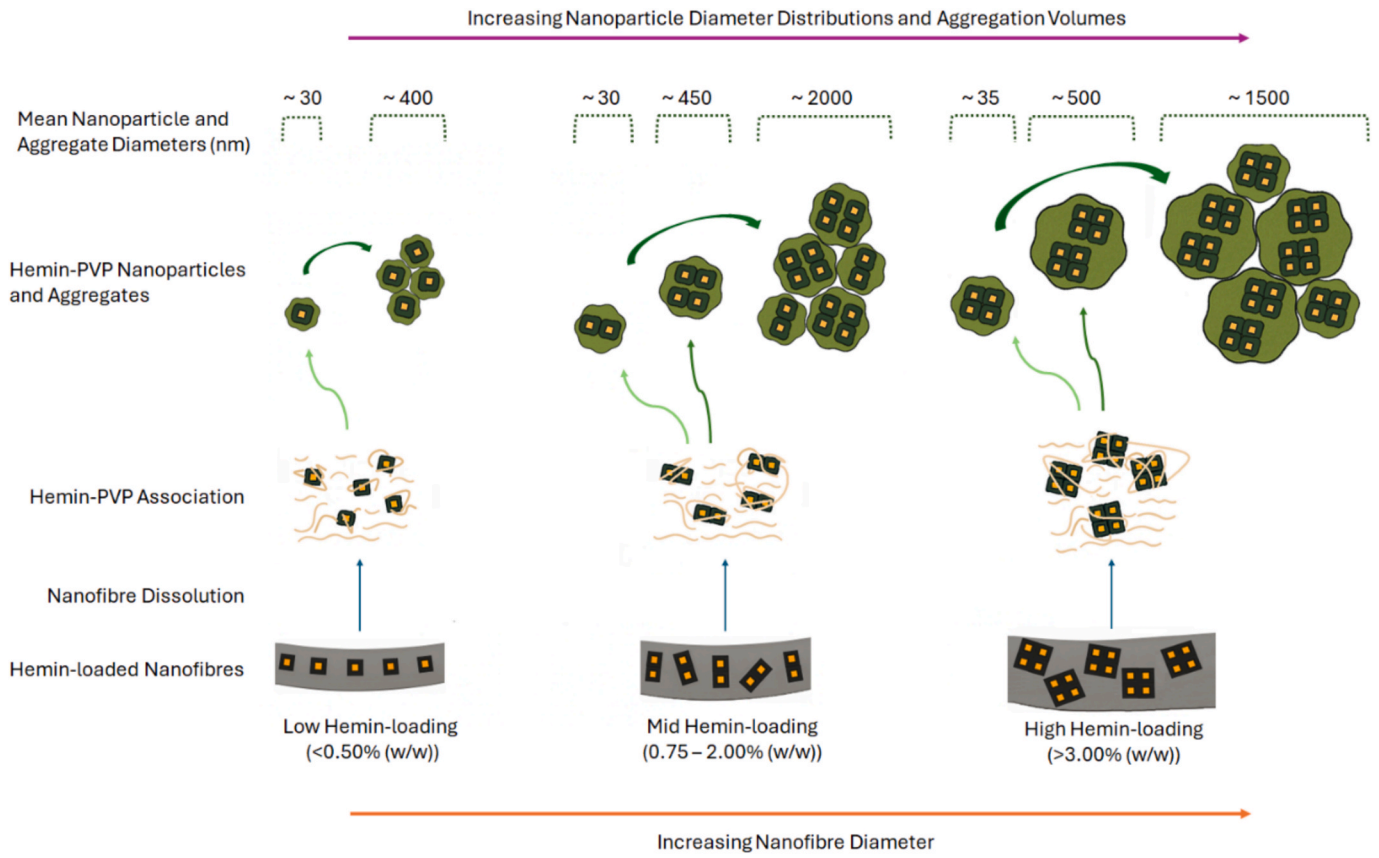

Fig. 12. A schematic illustration of hemin-PVP nanofibre dissolution in PBS and subsequent nanoparticle and aggregate formation. *Low hemin loading (≤0.50 % w/w, left)*: Narrow nanofibres with dispersed hemin form small hemin–PVP nanoparticles (~30 nm) that further associate into aggregates (~400 nm). *Medium loading (0.75–2.00 % w/w, middle)*: Hemin aggregation within the nanofibre creates larger nucleation sites upon dissolution, leading to bigger nanoparticles and aggregates. *High loading (≥3.00 % w/w, right)*: Extensive hemin aggregation produces even larger nucleation centres, forming individual nanoparticles (~450 nm) that aggregate into populations of ~ 1500 nm, while maintaining solubility in PBS.

4. Discussion

We report a novel formulation of hemin based on electrospun hemin–PVP fibres, which dissolve rapidly in physiological pH aqueous media to form nano- and micro-particles of hemin–PVP. This approach markedly enhances the solubility of hemin, achieving concentrations up to 273 μM. Previous strategies for oral hemin delivery have included coupling to iron oxide nanoparticles (average diameter 29 nm) (Jahn et al., 2011), complexation with γ-cyclodextrin (70 % encapsulation, 240-fold solubility enhancement) (Yu et al., 2024), and encapsulation into micelles (75–140 nm diameter, 25–60 % encapsulation, solubility up to 200 μM) (Span et al., 2016). All these formulations were evaluated in intestinal cell cultures for iron uptake or toxicity and showed promise in enhancing iron absorption (Jahn et al., 2011; Span et al., 2016; Yu et al., 2024).

Attempts to improve hemin solubility using PVP or other excipients yielded only 15.3 μM in neutral pH solutions (Inamura et al., 1989), requiring multiple steps including neutralisation with ammonia. In contrast, the electrospinning method offers a facile route to produce hemin–PVP fibres that dissolve rapidly in physiological buffers, making it an attractive strategy for enhancing hemin solubility.

Electrospun hemin fibres have also been developed by other groups for different applications. For instance, poly-3-hydroxybutyrate (PHB)-based fibres were designed for wound healing and antimicrobial activity (Tyubaeva et al., 2023), while polyacrylonitrile (PAN)-based fibres were used in electrocatalysis (Dong et al., 2020). Our PVP fibres incorporated hemin up to 5 % (w/w), a limit also reported for PHB fibres (Tyubaeva et al., 2023). PAC fibres contained up to 2 % (w/w) hemin (Dong et al., 2020). The PVP fibres in this study had smaller diameters (0.19–0.44 μm; Table S2.1, supplementary data) than PHB fibres (1.77–3.50 μm) (Nishide et al., 1977; Tyubaeva et al., 2021), but were larger than PAN fibres (0.10–0.20 μm) (Dong et al., 2020).

Hemin distribution within fibres was uniform in PVP and PAN (Dong et al., 2020), whereas PHB fibres showed homogeneous distribution only at 5 % (w/w) (Tyubaeva et al., 2021). At lower concentrations (1–3 % w/w), PHB fibres exhibited large hemin aggregates forming nodal structures (Tyubaeva et al., 2021), likely due to stronger interactions with the more crystalline PHB matrix. XRD analysis revealed that hemin tends to crystallize at low concentrations in both PVP (1 % w/w; Fig. 4) and PAN (2 % w/w) (Dong et al., 2020). The increasing hemin crystallinity at higher concentrations described here may explain the increased size of nanoparticles formed upon dissolution.

Hemin loading into PVP nanofibres, followed by the self-assembly of soluble hemin–PVP nanoparticles upon dissolution, shows promise as potential component of an oral formulation to treat iron deficiency anaemia. However, the effectiveness of hemin–PVP formulations as iron delivery vehicles remains to be determined. Future studies will focus on evaluating the bioavailability, cytotoxicity, uptake, and processing of soluble hemin nano- and micro-particles in cell culture models. Furthermore, it will be necessary to formulate the nanofibres platform further so that the hemin-PVP nanoparticles are released in a controlled manner for effective iron absorption.

Beyond this, two promising directions could expand the pharmaceutical utility of this platform. First, combining PVP-based fibres with other insoluble polymeric nanofibres in advanced architectures such as core–sheath or Janus structures could enable tailored drug release profiles, including sustained release, biphasic release, and even zero-order release for depot-like systems (Hu et al., 2025; Yang et al.,

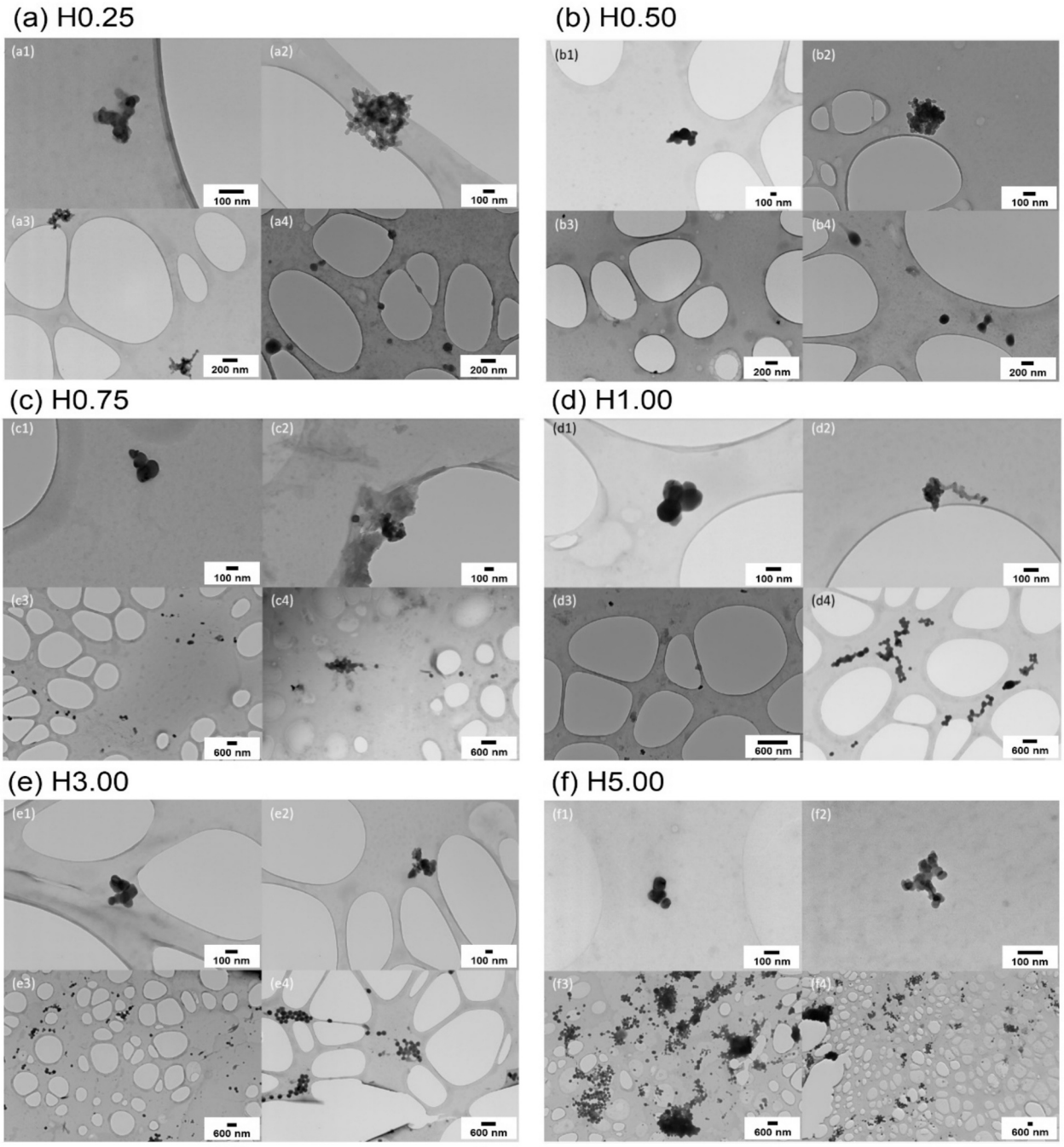

Fig. 13. TEM micrographs of nanoparticles from solutions of hemin-PVP fibres (a) H0.25, (b) H0.50, (c) H0.75, (d) H1.00 (e) H3.00 and (f) H5.00. Magnifications are: 2500x (c3, e3, f3), 4000x (c4, d4, e4), 8000x (a4, d3), 10000x (b3, b4), 12000x (a3, b1, e2), 15000x (c1, c2, f4), 20000x (a2, b2, d1, e1), 25000x (d2, f1), and 40000x (a1, f2). Individual nanoparticle diameters were measured using ImageJ with the scale calibrated to each micrograph scale bar, and the mean diameters calculated from n = ≥ 213 measurements.

2025; Yu et al., 2025). These designs have been widely explored for controlled release applications in electrospun systems, offering spatial separation of drug and excipients to modulate release kinetics (Yang et al., 2025).

Second, co-loading excipients such as lipids alongside hemin within the PVP matrix could promote self-assembly into liposomes or self-emulsifying structures upon dissolution, potentially enhancing transmembrane transport and improving oral absorption (Ge et al., 2023). Lipid-based excipients are well known to form colloidal structures in aqueous environments, improving solubilisation and facilitating lymphatic uptake, which can significantly enhance bioavailability of poorly soluble drugs (Mohite et al., 2023). These strategies align with current trends in nanofibre-based drug delivery systems and could significantly broaden the clinical applicability of electrospun formulations.

5. Conclusion

The potential to enhance the aqueous solubility of hemin through encapsulation in PVP nanofibres was investigated. The results demonstrated that a series of PVP-hemin nanofibres with differing loading were successfully prepared using a modified electrospinning approach.

Encapsulation efficiencies of 43–83 % were achieved, with increasing hemin crystallinity at higher loadings. Upon dissolution in PBS (pH 7.4), fibres dissolved within one hour, producing PVP-hemin nanoparticles primarily in the 10–80 nm range, alongside secondary populations of larger aggregates (200–2000 nm). In contrast, physical mixtures of hemin and PVP required over 72 h of stirring and yielding negligible sub–100 nm particles, instead forming aggregates predominantly >200 nm. The nanofibre formulations achieved a >200–fold increase (273 μM) in aqueous solubility relative to free hemin, surpassing all values reported with other solubilizing agents. This works demonstrates the potential of these electrospun materials as a component of an oral formulation for the treatment of iron deficiency anaemia. Future work will focus on the toxicity, cellular uptake and processing of the PVP-hemin nanoparticles reported in this study.

CRediT authorship contribution statement

Lewis R. Anderson: Writing – review & editing, Writing – original draft, Visualization, Validation, Project administration, Methodology, Investigation. **Erum Noureen:** Writing – review & editing, Methodology, Investigation. **Simon R. Collinson:** Writing – review & editing, Validation, Supervision, Formal analysis, Data curation. **Peter G. Taylor:** Writing – review & editing, Supervision, Formal analysis, Data curation. **Gemma C. Shearman:** Writing – review & editing, Supervision, Methodology, Investigation. **Katja Rietdorf:** Writing – review & editing, Validation, Supervision, Formal analysis. **Kenneth N. White:** Writing – review & editing, Writing – original draft, Supervision, Methodology, Investigation. **Nicholas P. Chatterton:** Writing – review & editing, Writing – original draft, Supervision, Project administration, Methodology, Investigation, Conceptualization.

Declaration of competing interest

The authors declare that they have no known competing financial interests or personal relationships that could have appeared to influence the work reported in this paper.

Acknowledgements

This work was financially supported by The Open University, including the provision of a PhD studentship for LA. The authors thank Timothy Barton of the Open University's School of Environment, Earth, and Ecosystem Sciences for conducting the ICP-OES measurements and Dr Zeeshan Mughal is thanked for his assistance with SEM images. All SEM and TEM work was performed at the Electron Microscopy Suite of The Open University, Milton Keynes, UK. The authors thank Prof. Gareth Williams for conducting XRD measurements at the School of Pharmacy, UCL.

Appendix A. Supplementary data

Supplementary data to this article can be found online at https://doi.org/10.1016/j.ijpharm.2025.126396.

Data availability

The data that supports the findings of this study are available from the corresponding author upon request.

References

Aljabri, M.D., Gosavi, N.M., Jones, L.A., Morajkar, P.P., La, D.D., Bhosale, S.V., 2019. Arginine-induced self-assembly of protoporphyrin to obtain effective photocatalysts in aqueous media under visible light. Molecules 24, 4172. https://doi.org/10.3390/molecules24224172.

Anderson, L.R., Hancox, C.C., Collinson, S.R., Rietdorf, K., Taylor, P.G., Chatterton, N.P., 2025. Improving the encapsulation of ferritin-like nanoparticles within polymeric nanofibers using a new electrospinning set-up and its effect upon iron release properties. Macromol. Mater. Eng. 310, 2400400. https://doi.org/10.1002/mame.202400400.

Auerbach, M., DeLoughery, T.G., Tirnauer, J.S., 2025. Iron deficiency in adults: a review. J. Am. Med. Assoc. 333, 1813–1823. https://doi.org/10.1001/jama.2025.0452.

Bailey, E.J., Winey, K.I., 2020. Dynamics of polymer segments, polymer chains, and nanoparticles in polymer nanocomposite melts: a review. Prog. Polym. Sci. 105, 101242. https://doi.org/10.1016/j.progpolymsci.2020.101242.

Batov, D.V., Kustov, A.V., Kruchin, S.O., Makarov, V.V., Berezin, D.B., 2019. Aggregation of cationic chlorin e6 derivatives in water and aqueous solutions of polyvinilpyrrolidone. J. Struct. Chem. 60, 443–448. https://doi.org/10.1134/S0022476619030120.

Benmore, C.J., Benmore, S.R., Wilke, S.K., Menon, V., Byrn, S.R., Weber, J.K.R., 2023. X-ray diffraction of water in polyvinylpyrrolidone. Mol. Pharm. 20, 3645–3652. https://doi.org/10.1021/acs.molpharmaceut.3c00265.

Castillo-Henríquez, L., Vargas-Zúñiga, R., Pacheco-Molina, J., Vega-Baudrit, J., 2020. Electrospun nanofibers: a nanotechnological approach for drug delivery and dissolution optimization in poorly water-soluble drugs. ADMET DMPK 8, 325–353. https://doi.org/10.5599/admet.844.

Charlebois, E., Pantopoulos, K., 2023. Nutritional aspects of iron in health and disease. Nutrients 15, 2441. https://doi.org/10.3390/nu15112441.

Dong, L., Zang, J., Wang, W., Liu, X., Zhang, Y., Su, J., Wang, Y., Han, X., Li, J., 2020. Electrospun single iron atoms dispersed carbon nanofibers as high performance electrocatalysts toward oxygen reduction reaction in acid and alkaline media. J. Colloid Interface Sci. 564, 134–142. https://doi.org/10.1016/j.jcis.2019.12.120.

Dong, R., Gong, W., Guo, Q., Liu, H., Yu, D.-G., 2024. Synergistic effects of radical distributions of soluble and insoluble polymers within electrospun nanofibers for an extending release of ferulic acid. Polymers 16, 2614. https://doi.org/10.3390/polym16182614.

Fütterer, S., Andrusenko, I., Kolb, U., Hofmeister, W., Langguth, P., 2013. Structural characterization of iron oxide/hydroxide nanoparticles in nine different parenteral drugs for the treatment of iron deficiency anaemia by electron diffraction (ED) and X-ray powder diffraction (XRPD). J. Pharm. Biomed. Anal. 86, 151–160. https://doi.org/10.1016/j.jpba.2013.08.005.

Galy, B., Conrad, M., Muckenthaler, M., 2024. Mechanisms controlling cellular and systemic iron homeostasis. Nat. Rev. Mol. Cell Biol. 25, 133–155. https://doi.org/10.1038/s41580-023-00648-1.

GBD 2021 Anaemia Collaborators, 2023. Prevalence, years lived with disability, and trends in anaemia burden by severity and cause, 1990-2021: findings from the Global Burden of Disease Study 2021. Lancet Haematol. 10, e713–e734. Doi: 10.1016/S2352-3026(23)00160-6.

Ge, R., Ji, Y., Ding, Y., Huang, C., He, H., Yu, D.-G., 2023. Electrospun self-emulsifying core-shell nanofibers for effective delivery of paclitaxel. Front. Bioeng. Biotechnol. 11. https://doi.org/10.3389/fbioe.2023.1112338.

Golnak, R., Xiao, J., Atak, K., Stevens, J.S., Gainar, A., Schroeder, S.L.M., Aziz, E.F., 2015. Intermolecular bonding of hemin in solution and in solid state probed by N K-edge X-ray spectroscopies. PCCP 17, 29000–29006. https://doi.org/10.1039/C5CP04529K.

Greiner, A., Wendorff, J.H., 2007. Electrospinning: a fascinating method for the preparation of ultrathin fibers. Angew. Chem. Int. Ed. 46, 5670–5703. https://doi.org/10.1002/anie.200604646.

Hooda, J., Shah, A., Zhang, L., 2014. Heme, an essential nutrient from dietary proteins, critically impacts diverse physiological and pathological processes. Nutrients 6, 1080–1102. https://doi.org/10.3390/nu6031080.

Hotaling, N.A., Bharti, K., Kriel, H., Simon, C.G., 2015. DiameterJ: a validated open source nanofiber diameter measurement tool. Biomaterials 61, 327–338. https://doi.org/10.1016/j.biomaterials.2015.05.015.

Hu, Y., Zhang, F., Zhou, J., Yang, Y., Ding, D., Li, M., Wang, C., Wang, B., Yu, J., Jiang, F., Yu, D.-G., Shen, H., 2025. Electrospun tri-layer core-sheath nanofibrous coating for sequential treatment of postoperative complications in orthopedic implants. Small 21, e05523. https://doi.org/10.1002/smll.202505523.

Inamura, I., Isshiki, M., Araki, T., 1989. Solubilization of hemin in neutral and acidic aqueous solutions by forming complexes with water-soluble macromolecules. Bull. Chem. Soc. Jpn 62, 2413–2415. https://doi.org/10.1246/bcsj.62.2413.

Jahn, M.R., Shukoor, I., Tremel, W., Wolfrum, U., Kolb, U., Nawroth, T., Langguth, P., 2011. Hemin-coupled Iron(III)-hydroxide nanoparticles show increased uptake in caco-2 cells. J. Pharm. Pharmacol. 63, 1522–1530. https://doi.org/10.1111/j.2042-7158.2011.01356.x.

Kale, K.S., Shinde, S.B., 2024. Solubility enhancement of poorly soluble drug. Int. J. Pharm. Sci. 2, 463–487. https://doi.org/10.5281/zenodo.12679933.

Lee, K.H., Khan, F.N., Cosby, L., Yang, G., Winter, J.O., 2021. Polymer concentration maximizes encapsulation efficiency in electrohydrodynamic mixing nanoprecipitation. Front. Nanotechnol. 3. https://doi.org/10.3389/fnano.2021.719710.

Mishra, R.K., Datt, M., Banthia, A.K., 2008. Synthesis and characterization of pectin/PVP hydrogel membranes for drug delivery system. AAPS PharmSciTech 9, 395–403. https://doi.org/10.1208/s12249-008-9048-6.

Mohite, P., Singh, S., Pawar, A., Sangale, A., Prajapati, B.G., 2023. Lipid-based oral formulation in capsules to improve the delivery of poorly water-soluble drugs. Front. Drug Deliv. 3. https://doi.org/10.3389/fddev.2023.1232012.

Morrison, D.B., Williams, E.F., 1941. The solubility and titration of hemin and ferrihemic acid. J. Biol. Chem. 137, 461–473. https://doi.org/10.1016/S0021-9258(19)56151-8.

Nath, A., Dharmadhikari, J.A., Dharmadhikari, A.K., Mathur, D., Mazumdar, S., 2017. Ultrafast dynamics of hemin aggregates. PCCP 19, 26862–26869. https://doi.org/10.1039/C7CP04858K.

Nishide, H., Mihayashi, K., Tsuchida, E., 1977. Dissociation of aggregated ferroheme complexes and protoporphyrine IX by water-soluble polymers. Biochim. Biophys. Acta BBA - Gen. Subj. 498, 208–214. https://doi.org/10.1016/0304-4165(77)90100-3.

Obeagu, E.I., Prajapati, S.K., Maurya, S.D., 2025. Anemia in pregnancy: the role of iron transport and regulation. Int. J. Med. Sci. Pharma Res. 11, 21–27. https://doi.org/10.22270/ijmspr.v11i1.136.

Omer, S., Forgách, L., Zelkó, R., Sebe, I., 2021. Scale-up of electrospinning: market overview of products and devices for pharmaceutical and biomedical purposes. Pharmaceutics 13, 286. https://doi.org/10.3390/pharmaceutics13020286.

Pantopoulos, K., 2024. Oral Iron supplementation: new formulations, old questions. Haematologica 109, 2790–2801. https://doi.org/10.3324/haematol.2024.284967.

Parmar, K., Patel, R., 2025. Novel nano-technologies to enhance drug solubility, dissolution and bioavailability of poorly water-soluble drugs. Biomater. Connect 2, 1–10.

Paul, S., Selvam, S., Heng, P.W.S., Chan, L.W., 2013. Elucidation of monomerization effect of PVP on Chlorin e6 aggregates by spectroscopic, chemometric, thermodynamic and molecular simulation studies. J. Fluoresc. 23, 1065–1076. https://doi.org/10.1007/s10895-013-1236-4.

Said, E.Z., Al-Sammerrai, D., 1985. Thermal decomposition of haemin chloride and related derivatives. J. Anal. Appl. Pyrol. 9, 35–41. https://doi.org/10.1016/0165-2370(85)80004-8.

Shah, H.E., Bhawnani, N., Ethirajulu, A., Alkasabera, A., Onyali, C.B., Anim-Koranteng, C., Mostafa, J.A., 2021. Iron deficiency-induced changes in the hippocampus, corpus striatum, and monoamines levels that lead to anxiety, depression, sleep disorders, and psychotic disorders. Cureus 13, e18138. https://doi.org/10.7759/cureus.18138.

Siegert, S.W.K., Holt, R.J., 2008. Physicochemical properties, pharmacokinetics, and pharmacodynamics of intravenous hematin: a literature review. Adv. Ther. 25, 842–857. https://doi.org/10.1007/s12325-008-0094-y.

Span, K., Verhoef, J.J.F., Hunt, H., van Nostrum, C.F., Brinks, V., Schellekens, H., Hennink, W.E., 2016. A novel oral iron-complex formulation: encapsulation of hemin in polymeric micelles and its *in vitro* absorption. Eur. J. Pharm. Biopharm. 108, 226–234. https://doi.org/10.1016/j.ejpb.2016.09.002.

Stec, D.E., Hinds, T.D., 2020. Natural product heme oxygenase inducers as treatment for nonalcoholic fatty liver disease. Int. J. Mol. Sci. 21, 9493. https://doi.org/10.3390/ijms21249493.

Suzuki, M., Nakata, K., Kuroda, R., Kobayashi, T., Tokunaga, E., 2016. Electrooptic Kerr effect of porphyrin H-aggregates in polymer films: polymer specific spectral blue Shift. Chem. Phys. 469–470, 88–96. https://doi.org/10.1016/j.chemphys.2016.02.002.

Taylor, L.S., Zografi, G., 1997. Spectroscopic characterization of interactions between PVP and indomethacin in amorphous molecular dispersions. Pharm. Res. 14, 1691–1698. https://doi.org/10.1023/A:1012167410376.

Topuz, F., Uyar, T., 2025. Recent developments in nanofiber-based fast-disintegrating drug delivery systems. Expert Opin. Drug Deliv. 22, 957–969. https://doi.org/10.1080/17425247.2025.2497831.

Tsvetkov, V.B., Solov'eva, A.B., Melik-Nubarov, N.S., 2014. Computer modeling of the complexes of Chlorin e6 with amphiphilic polymers. Phys. Chem. Chem. Phys. PCCP 16, 10903–10913. https://doi.org/10.1039/c3cp55510k.

Tyubaeva, P., Varyan, I., Lobanov, A., Olkhov, A., Popov, A., 2021. Effect of the hemin molecular complexes on the structure and properties of the composite electrospun materials based on poly(3-hydroxybutyrate). Polymers 13, 4024. https://doi.org/10.3390/polym13224024.

Tyubaeva, P.M., Varyan, I.A., Gasparyan, K.G., Romanov, R.R., Yurina, L.V., Vasilyeva, A.D., Popov, A.A., Arzhakova, O.V., 2024. Life cycle of functional all-green biocompatible fibrous materials based on biodegradable polyhydroxybutyrate and hemin: synthesis, service life, and the end-of-life via biodegradation. ACS Appl. Bio Mater. 7, 2325–2337. https://doi.org/10.1021/acsabm.4c00010.

Tyubaeva, P.M., Varyan, I.A., Krivandin, A.V., Shatalova, O.V., Olkhov, A.A., Popov, A. A., Xu, H., Arzhakova, O.V., 2023. Structure and performance of all-green electrospun PHB-based membrane fibrous biomaterials modified with hemin. Membranes 13, 478. https://doi.org/10.3390/membranes13050478.

Vass, P., Szabó, E., Domokos, A., Hirsch, E., Galata, D., Farkas, B., Démuth, B., Andersen, S.K., Vigh, T., Verreck, G., Marosi, G., Nagy, Z.K., 2020. Scale-up of electrospinning technology: applications in the pharmaceutical industry. Wiley Interdiscip. Rev. Nanomed. Nanobiotechnol. 12, e1611.

Xudayberganov, N.Y., Jabbarov, M.T., Matyoqubov, M.O., 2017. Neurological symptoms of severe level iron deficient anemia patients. Natl. J. Neurol. 2017, 54–56. https://doi.org/10.61788/njn.spec.17.07.

Yang, X., Wang, Q., Zhu, Z., Lu, Y., Liu, H., Yu, D.-G., Bligh, S.-W.-A., 2025. A modified triaxial electrospinning for a high drug encapsulation efficiency of curcumin in ethylcellulose. Pharmaceutics 17, 1152. https://doi.org/10.3390/pharmaceutics17091152.

Yu, D.-G., He, W., He, C., Liu, H., Yang, H., 2025. Versatility of electrospun Janus wound dressings. Nanomed 20, 271–278. https://doi.org/10.1080/17435889.2024.2446139.

Yu, D.-G., Li, J.-J., Williams, G.R., Zhao, M., 2018. Electrospun amorphous solid dispersions of poorly water-soluble drugs: a review. J. Control. Release off. J. Control. Release Soc. 292, 91–110. https://doi.org/10.1016/j.jconrel.2018.08.016.

Yu, Q., Huang, L., Zhang, Y., Teng, W., Wang, Y., Cao, J., Wang, J., 2024. Intestinal-targeted digestion of heme chloride by forming inclusion complexes in vitro. Foods 13, 3078. https://doi.org/10.3390/foods13193078.